PAPER

Role of sulphur in resistive switching behavior of natural rubber-based memory

IOP Publishing Nanotechnology

Nanotechnology **36** (2025) 035201 (19pp) https://doi.org/10.1088/1361-6528/ad8890

Role of sulphur in resistive switching behavior of natural rubber-based memory

Muhammad Awais[1], **Nadras Othman**[2], **Mohamad Danial Shafiq**[2], **Feng Zhao**[3,*] and **Kuan Yew Cheong**[1,*]

[1] Electronic Materials Research Group, School of Materials & Mineral Resources Engineering, Engineering Campus, Universiti Sains Malaysia, 14300 Nibong Tebal, Seberang Perai Selatan, Pulau Pinang, Malaysia
[2] School of Materials & Mineral Resources Engineering, Engineering Campus, Universiti Sains Malaysia, 14300 Nibong Tebal, Seberang Perai Selatan, Pulau Pinang, Malaysia
[3] Micro/Nanoelectronic and Energy Laboratory, School of Engineering and Computer Science, Washington State University, Vancouver, WA 98686, United States of America

E-mail: feng.zhao@wsu.edu and srcheong@usm.my

Received 21 May 2024, revised 23 July 2024
Accepted for publication 18 October 2024
Published 28 October 2024

Abstract

The rising environmental awareness has spurred the extensive use of green materials in electronic applications, with bio-organic materials emerging as attractive alternatives to inorganic and organic materials due to their natural biocompatibility, biodegradability, and eco-friendliness. This study showcases the natural rubber (NR) based resistive switching (RS) memory devices and how varying sulphur concentrations (0–0.8 wt.%) in NR thin films impact the RS characteristics. The NR was formulated and processed into a thin film deposited on an indium tin oxide substrate as the bottom electrode and with an Ag film as the top electrode. The addition of sulphur modifies the degree of crosslinking in the NR thin film, from which the concentration of –C=C– group and density of defect site (S^+) are affected, and hence the RS behavior of the memory device. The devices exhibit bipolar resistance with symmetric switching characteristics which are attributed to the formation of conductive paths facilitate by electron transport along –C=C– and S^+ defect sites between the two electrodes. Notably, a sample with 0.2 wt.% sulphur exhibits a high ON/OFF ratio (10^4), a large memory window (5.5 V), prolonged data retention (10 yrs), and reliable endurance (120 cycles). These findings highlight the potential of NR as a promising material for eco-friendly resistive-switching random access memory applications.

Keywords: sulphur, natural rubber, crosslinking, resistive-switching memory

1. Introduction

Nonvolatile memory devices have become an essential feature in many advanced electronic systems to facilitate the anticipated information explosion in the internet of things era. Conventional memories are based on charge storage in a floating-gate transistor, which follows Moore's law downscaling trend to enhance density and device performance [1–4]. However, when transistors are downscaled below the sub-nanometer range, the trend becomes unsustainable due to several essential and technical restrictions that result in diminishing downsizing benefits [5–9]. Next-generation nonvolatile memories ought to operate based on innovative concepts that

* Authors to whom any correspondence should be addressed.

differ from typical charge storage in floating-gate transistors to enable advancement over the long term. Electrically monitored resistive switching (RS) behaviors in metal-insulator-metal (MIM) structures could constitute an exciting concept for redefining the boundaries of next-generation nonvolatile memories among emerging storage principles. This approach provides potential benefits in numerous important domains, including down-scalability, fabrication cost, power consumption, and switching speed [10–17]. RS has been demonstrated in a wide range of inorganic [18–20] and organic [21–23] materials that are typically deposited as a continuous thin film sandwiched between two conducting electrodes to form a MIM structure. However, careful consideration should be exercised during the manufacturing process because the deposition of these materials employs various power-demanding processes (e.g. chemical vapor deposition, thermal evaporation, and molecular beam epitaxy) that can result in an energy-imbalance scenario [24, 25]. Furthermore, the use of materials produced from nonrenewable resources (e.g. fossil fuels and mined minerals) can raise serious concerns about sustainability. In general, these materials are chemically resilient, necessitating an endlessly long period of natural disintegration after disposal, leaving vast amounts of electronic trash in landfills across the globe [26–29].

With growing ecological consciousness and the proliferation of disposable gadgets, there is an urgent need to develop new electronic applications based on greener bio-organic materials, that usually come from living (or once-living) organisms found in nature. Bio-organic materials are not only sustainable, biocompatible, and ecologically friendly with a goal to provide a long-term solution to environmental challenges, but they are also exotic for next-generation electronic manifestation [30–33]. RS behaviors observed in numerous bio-organic MIM devices have been attracting a lot of interest, since its first reported using virus as the memristive layer in 2006 [31, 34–38]. Different names for the same-structured memory devices are used; among the most common names are bio-memristor and resistive random-access memory (ReRAM). In general, the RS properties of bio-organic-based ReRAMs include memory window, endurance cycle, ON/OFF ratio, and retention time strongly depend on the formation and rupture of conductive pathways by means of different RS mechanisms [3, 39–42]. The conductive paths consist of carriers hopping within defect sites, metallic filaments formation due to redox process, and/or carbon phase transformation of sp^3 to sp^2 due to absorption of thermal energy or chemical reaction within the bio-organic memristive layers. Typically, the rupturing of the conductive paths are governed by annihilation of defect sites, breakage of metallic filaments due to Joule heating and/or carbon phase transformation from sp^2 to sp^3. These RS mechanisms are strongly depending on type and dimension of both top and bottom electrodes (BEs), type of bio-organic material as the memristive layer, type of entities (ionic compounds, metallic nanoparticles, carbon derived nanostructures, etc.) loaded in the bio-organic material, memristive layer processing methods, and electrical measurement techniques [43–47]. The previously reported RS characteristics of bio-organic-based devices were gathered and nicely reviewed [14, 48–50]. The RS characteristics of these natural materials-based devices, such as read memory window, ON/OFF ratio, form voltage, and endurance were within the range of 0.1–21.9 V, 10^1–$10^{7,}$ 1.2–9 V, and 10^1–10^3 cycles, respectively [3, 48, 51, 52].

Till now, several bio-organic materials including polypeptides, polysaccharides, viruses, and plant extracts were reported [53, 48, 49, 51, 54–58]. The research on these bio-organic materials is still ongoing aiming to further improve the RS performance for various memory applications. To further expand this list, we investigated a new natural rubber (NR)-based bio-organic material for RS memory applications. NR, extracted from Hevea brasiliensis is a colloidal structure composed of poly-cis-1,4-isoprene particles scattered in an aqueous serum. It is having approximately 60% water, 35% cis-1,4-polyisoprene, and 5% non-isoprene molecules, where non-isoprene mainly consists of proteins, lipids, carbohydrates, and minerals [59, 60]. NR is a class of polyisoprenoids which is one of the eight essential biopolymer groups synthesized by living organisms. Polyisoprenoids are derivatives of isoprene (2-methyl-1,3-butadiene), a long chain of molecules that contains repeating subunits, and have a methyl-branched carbon-carbon backbone in their chemical structure [61, 62]. Previously, NR-based resin has been employed as reliable electrical insulators for various applications [63, 64]. In contrast, electrical conductivity of NR can be increased by loading with metallic particles in different concentration, size and form factor, by varying type and density of cross-linkers, and by optimizing on the vulcanization parameters such as time and temperature. Among these parameters, the type of cross-linker and cross-linking density are expected to be the most important factors affecting the structure of the conductive paths. It was also reported that increasing the rate of cross-linking during the vulcanization process may also increase the electrical conductivity of NR [65, 66]. Furthermore, the cross-linking density is associated with the type of cross-linker used. Sulphur is one of the most commonly used cross-linking agents that can bond chemically with polyisoprene to form long chains that is known as polysulphide. Several investigations demonstrate that the electrical and mechanical properties of NR were largely influenced by changing the composition of sulphur as a cross-linker [67].

With these promising features of NR in electronic applications, it built our interest to explore its potential for RS memory applications and investigate the influence of cross-linker on its characteristics for the first time. The evidence of a non-volatile bipolar switching memory in NR by changing the concentration of sulphur in the NR latex is revealed with the mechanism governing the RS behavior is proposed. This work demonstrates a high ON/OFF ratio in the order of 10^4 at a lower read voltage of 0.25 V, and a large memory window of 5.5 V. The retention and endurance characteristics of the memory device are investigated as well to evaluate the reliability of the memory device. The fabricated NR-based device exhibits consistent and competitive performance demonstrating its potential for non-volatile memory applications.

Table 1. Formulation of the natural rubber compounding latex.

Ingredients	Function	Part by mass		
		Dry weight (pphr)	Actual weight (pphr)	Compound weight (g)
60% NR HA Latex	Raw material	100.00	166.6	286.66
10% KOH	pH modifier	0.30	3.00	5.16
20% Potassium Oleate	Stabilizer	0.25	1.25	2.15
50% Sulphur	Vulcanizing agent	0.2	0.40	0.86
50% ZDEC	Accelerator	0.75	1.50	2.58
50% ZnO	Activator	0.25	0.50	0.86
50% Antioxidant 2,2-methylene-bis (4-methyl-6-tert-butylphenol)	Antioxidant	0.50	1.00	1.72
Total		102.25	174.25	299.99

2. Experimental section

2.1. Compounding of NR latex

Commercial NR latex (poly 1,4-cis-isoprene) or centrifuged latex (60% dry rubber content) with high ammonia was obtained from Zarm Scientific and Supplies SDN. BHD. Malaysia. The obtained latex was compounded with ingredients weighed based on the predefined formulation as shown in table 1. The slurry solution was prepared by mixing potassium hydroxide (KOH), potassium oleate, sulphur (S), zinc diethyldithiocarbamate (ZDEC), zinc oxide (ZnO), and antioxidant (2,2-methylene-bis(4-methyl-6-tert-butylphenol)). The slurry solution is then added to NR high ammonia latex and stirred continuously for one hour at room temperature. The compounded latex is then pre-vulcanized for around 30 mins by heating the latex in the water bath maintained at 70 °C. The compounded latex is stirred continuously using a mechanical stirrer to avoid skin formation and sedimentation of ingredients. Then, a chloroform number test was performed by taken 5 ml of latex from the compounded latex every five mins and mixed with 5 ml of chloroform. The pre-vulcanization step was stopped after reaching chloroform number 3. The process was repeated four more times by varying the concentration of sulphur (0 wt.%, 0.2 wt.%, 0.4 wt.%, 0.6 wt.%, and 0.8 wt.%). The pre-vulcanized NR latex was placed outside for maturation for one day. Figures 1(a) and (b) shows the NR latex with ammonia, alongside the compounded solutions that were subsequently prepared.

3. Device fabrication

The structure of the NR-based devices has been fabricated according to the cross-section illustrated in figure 1(d). The substrate for the device was made of indium tin oxide (ITO)-coated glass (sheet resistance $\leqslant 7\ \Omega\ \square^{-1}$, ITO thickness $= 220 \pm 30$ nm) from Zhuhai Kaivo Optoelectronic Technology Co., China. The substrate was cut into smaller dimensions (2×2 cm) with the help of a diamond cutter. The substrates were cleaned using the detergent-solvent cleaning process, which involves immersing each substrate for 15 mins in a separate ultrasonic bath (Elmasonic S 30 H, Elma) with acetone (CMOS grade, J.T. Baker, Philipsburg, NJ, USA), ethanol (95 v/v%, Merck Millipore, Burlington, MA, USA), and deionized water. A 200 μl of the pre-vulcanized NR latex was then spin-coated onto the clean ITO glass substrate by a micropipette (Pipetman Classic P1000, Gilson) at 3000 rpm for 30 s. The same steps were repeated for all samples with different concentrations of sulphur as mentioned before. The samples were then cured in an oven (UFB 400, Memmert) at 180 °C for 30 mins. The NR-based thin film solidified after cooling to room temperature. Finally, an array of 100 nm thick Ag was thermally evaporated (K950X, Quorum Emitech, UK) at a base pressure of approximately 10^{-4} Torr on top of the NR thin film as a top electrode. The evaporation process was carried out using Ag wire (>99.99%, 0.2 mm diameter, Stanford Advanced Materials, USA). The top electrodes of the device were patterned using a metal mask (Choon Automech, Penang, Malaysia) with arrays of 0.08 cm diameter. The calculated area of the device, which corresponds to the area of the top electrode was 5.03×10^{-3} cm^2. Figure 1(c) shows the top view of a fabricated device with array of top electrode and figure 1(d) presents the schematic cross-sectional view of the device. Typical surface morphology measured by field emission scanning electron microscope (FESEM) (Hitachi SFE-SEM SU8700) of the dried NR thin film is shown in figures 1(e) and (f) with a magnification scale of 100 nm and 1 μm, respectively. The thickness of the dried NR thin film was $\sim$150 μm determined by FESEM from the cross-sectional view of the sample (figure 1(g)) Energy dispersive x-ray spectroscopy (EDS) analysis of the NR thin film is shown in figure 1(h). The presence of carbon, oxygen, and sulphur is consistent with the NR matrix, while other trace elements were considered as impurities during compounding and formulation of the NR.

3.1. Fourier transform infrared (FTIR) spectroscopy

The chemical functional groups in NR-based thin films and the formulated precursor solutions were investigated by a FTIR spectrometer (PerkinElmer Spectrum One, Waltham, MA,

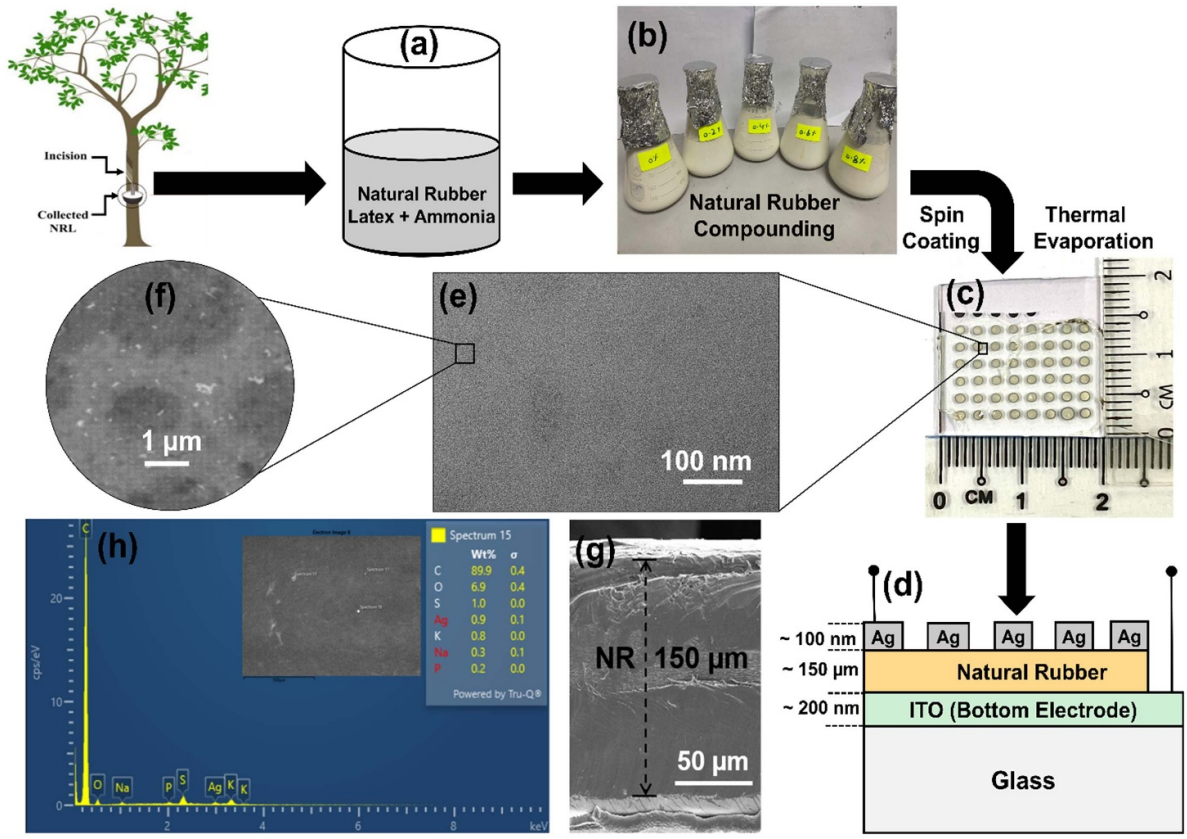

Figure 1. (a) Graphic of natural rubber latex collected from rubber tree, (b) photograph of the compounded latex solutions with different sulphur concentrations, (c) optical image of complete device structure, (d) schematic cross-sectional view of a natural rubber based MIM test structure, SEM image of a dried natural rubber surface with a magnification scale of (e) 10 nm, (f) 1 μm, (g) cross-sectional view of the natural rubber based MIM test structure captured using FESEM, and (h) EDS analysis of the natural rubber surface.

USA). A dried NR film was placed on the ZnSe crystal window (Cat. No. Z2691, Sigma-Aldrich, St. Louis, MO, USA) for all the measurements. The formulated liquid precursor was dropped in a volume of 10 ml onto the crystal window. A background scan was carried out on a blank ZnSe crystal window before acquiring the FTIR spectrum to offset any infrared absorption resulted due to the crystal window. The FTIR spectrum of each measurement was acquired 128 times using the transmittance mode in the range of 4000–500 cm^{-1} with a resolution of 4 cm^{-1}.

3.2. High-resolution transmission electron microscopy-energy dispersive x-ray spectroscopy (HRTEM-EDS)

The HRTEM (Tecnai G^2 F20 X-Twin, FEI, Hillsboro, OR, USA) was used to characterize the morphology and cross-sectional view of NR-based thin film at 200 keV. EDS (X-Max^N 80 T, Oxford Instruments, Abingdon, United Kingdom) in HRTEM was used to determine the elemental chemical composition. An advanced Helios NANOLAB 650 Dual Beam microscope (FEI, Hillsboro, OR, USA), equipped with a Ga ion source in the focused ion beam column was used for the lamella sample preparation. An omniprobe needle was used to place the prepared lamella sample. The sample was coated with a platinum via sputter coater to minimize the charging effect. Platinum (Pt) ion beam was deposited onto the interest region for protection from Ga ion beam bombardment prior to lamella preparation. The lamella was prepared by in-situ lift out technique using Dual Beam equipment. The lamella was mounted onto Copper (Cu) grid and thinned down to less than 100 nm prior to TEM EDS analysis.

3.3. Atomic force microscopy (AFM)

The surface topography and roughness of the NR thin films with different concentrations of sulphur were characterized by NanoNavi SPA 300-HV (Hitachi High-Tech Science Corporation, Chiba, Japan) AFM. The surface topography and phase imaging were determined subsequently by a Tap300Al-G cantilever (Budget Sensors, Sofia, Bulgaria) operated in the tapping mode. The cantilever tip has an appearance like a rotating cone with a diameter of less than 20 nm and a half-cone angle of rotation that was roughly 20° from the cantilever axis, 25° from both sides, and 10° from the apex. The cantilever's force constant and resonance frequency are 40 N m^{-1} and 300 kHz. The following equations were used to determine the

average (R_a) and root-mean-square (R_{rms}) surface roughness with a proprietary SPIWin software (v5.01 C).

4. Thermal analysis

The impact of heating temperature on the weight loss of NR latex was investigated through thermogravimetric analysis (TGA) (Pyris 6 Perkin Elmer thermogravimetric analyzer). In a typical measurement, 10 mg of NR latex was carefully placed in a high-tension alumina heating pan within the measurement chamber and tested with a heating rate of 10 °C min^{-1}. The assessment involved monitoring the weight loss of the NR latex precursor solution as it underwent heating from room temperature to 600 °C in nitrogen atmosphere at a flow rate of 20 ml min^{-1}.

5. Device characterization

A Semiconductor Parameter Analyzer (4156C, Agilent, Santa Clara, CA, USA) was used to investigate the RS behaviors of the devices under ambient conditions. The device was placed on a probe station (PE-2, Everbeing Int'l Corp., Taiwan) with two movable needles which were connected to the semiconductor parameter analyzer and controlled by Metrics ICS v3.6 software. For all measurements, the bias voltage was applied on the top electrode of the device while the BE was always grounded. Both the compliance current and the DC voltage sweep were kept at 1 mA and 0.5 V s^{-1}, respectively. To assess device-to-device stability, five separate samples were prepared, and electrical characterization was conducted on each.

6. Results and discussion

The phases of NR-based thin film deposited on an ITO/glass substrate were determined by XRD as shown in figure 2. The x-ray diffraction pattern exhibits two significant peaks at 2θ values of approximately 31° and 36° that are associated to the substrate of ITO [68, 69] and a strong diffraction peak at 39° that is belonging to Ag (111) of the top metal electrode [70]. A broad diffraction peak at the background of those three diffraction peaks is clearly recorded and it is attributed to amorphous nature of the NR [71]. Figure 3 shows the FTIR transmittance spectra of a typical NR precursor solution with various sulphur concentrations in wt.%. The samples in all precursors show a broad peak at 3365 cm^{-1}, which is attributed to hydroxyl (–OH) group and it belongs to the residues of amino acids, proteins, fatty acids, and/or moisture absorbed by the more polar matrix presents in the NR latex. Absorption bands at 2953 cm^{-1} and 2850 cm^{-1} are assigned to the symmetrical and asymmetrical stretching of the CH_3 methyl group and the aliphatic C–H stretching from the $–CH_2$ group, respectively, while absorption bands at 1450 cm^{-1} and 1370 cm^{-1} can be attributed to the symmetric and asymmetric deformation of the $–CH_2$ and $–CH_3$ groups, respectively in the NR latex as shown

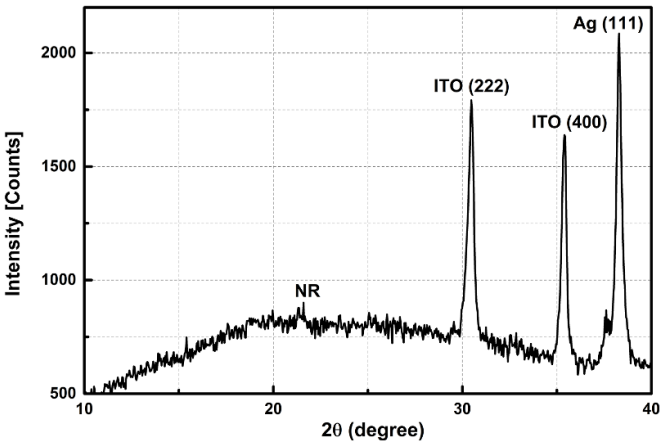

Figure 2. XRD diffraction pattern of a natural rubber thin film dried at 100 °C on ITO substrate.

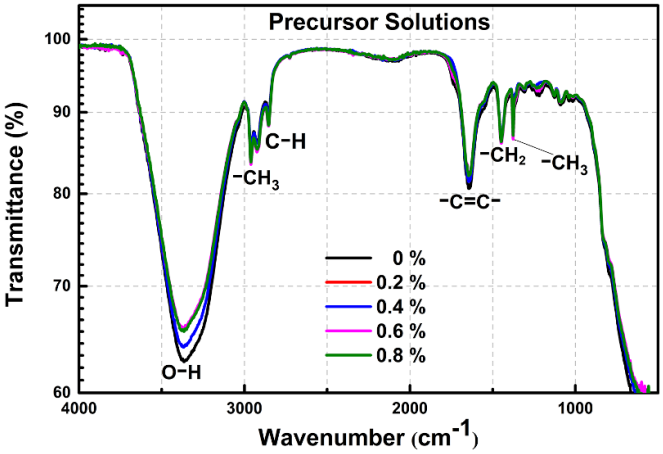

Figure 3. FTIR transmittance spectra of natural rubber latex precursor solutions with different sulphur concentrations.

in the chemical structure of figure 4. In addition, an absorption band at 1640 cm^{-1}, which is assigned to –C=C– stretching from an alkene group in the NR latex is also recorded in the FTIR spectra. These characteristic absorption bands with their assigned functional groups in the latex solutions of this work is in agreement with the typical reported NR latex functional groups [71, 72].

By adding sulphur in the precursor solution of NR (polyisoprene) in the pre-vulcanization stage (sequence ① in figure 5), –C=C– within the isoprene reacts with sulphur via polarization process [66, 73] to form sulphur anions (S_n^-) or it is known as polarized sulphur (②). Specifically, the sulphur anions are likely to engage either with –CH bond or directly with the carbon atoms. The –C=C– bond exhibits a higher level of reactivity if compared to –CH [66, 74] by breaking off the –C=C– bond which leads to the formation of carbocation (C^+) (③). These positively charged carbocation provides a reactive site for interacting with S_n^- and resulted in crosslinking with the generation of sulfonium ion (S^+) (④). These sulfonium ions

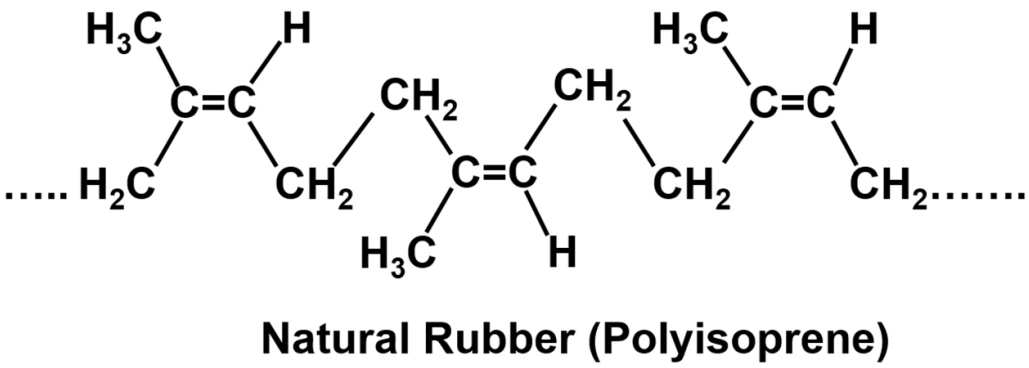

Figure 4. Typical chemical structure of natural rubber in precursor solution [73].

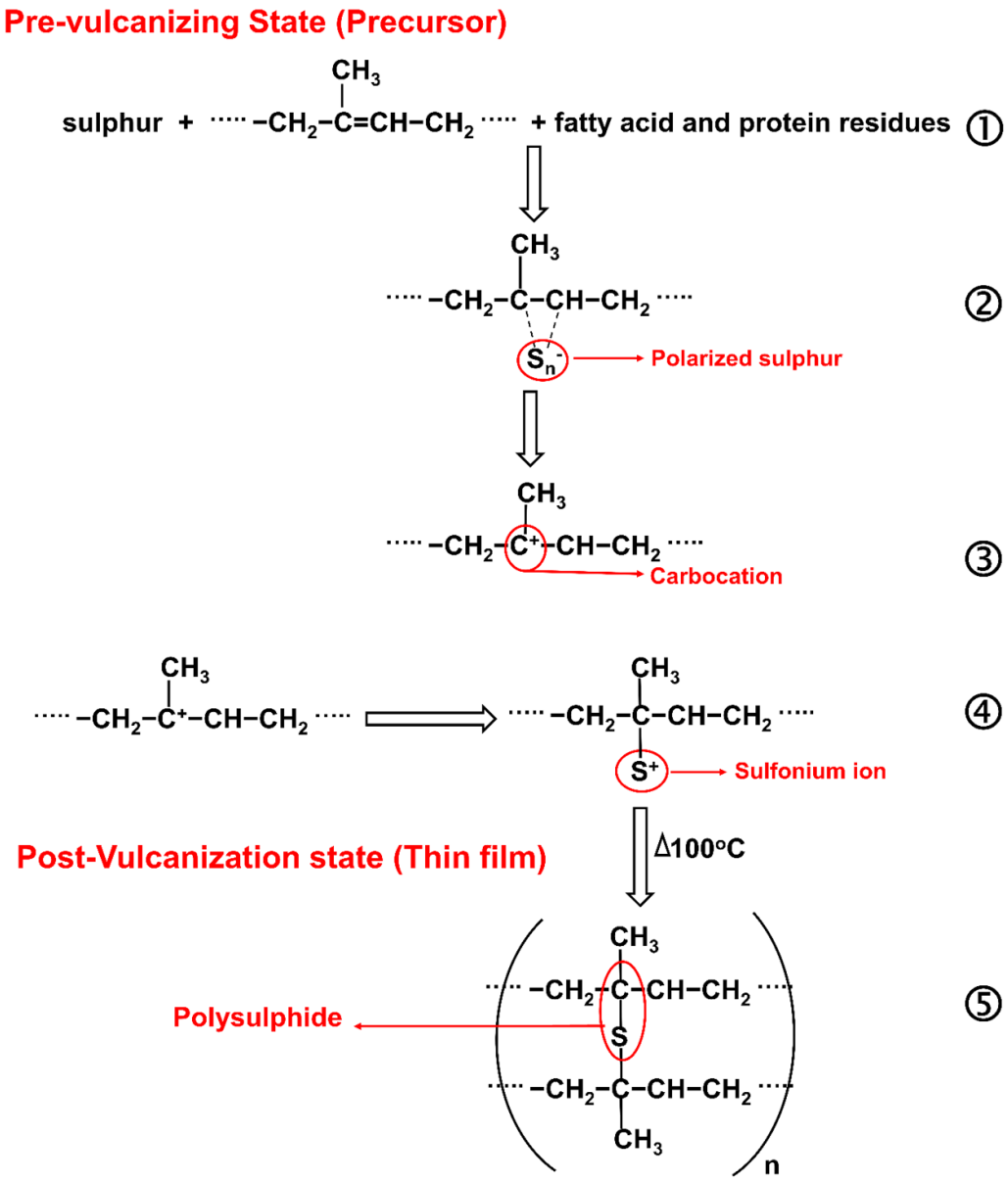

Figure 5. Schematic representation of the vulcanization process of natural rubber, showing the transition from precursor to post-vulcanization states.

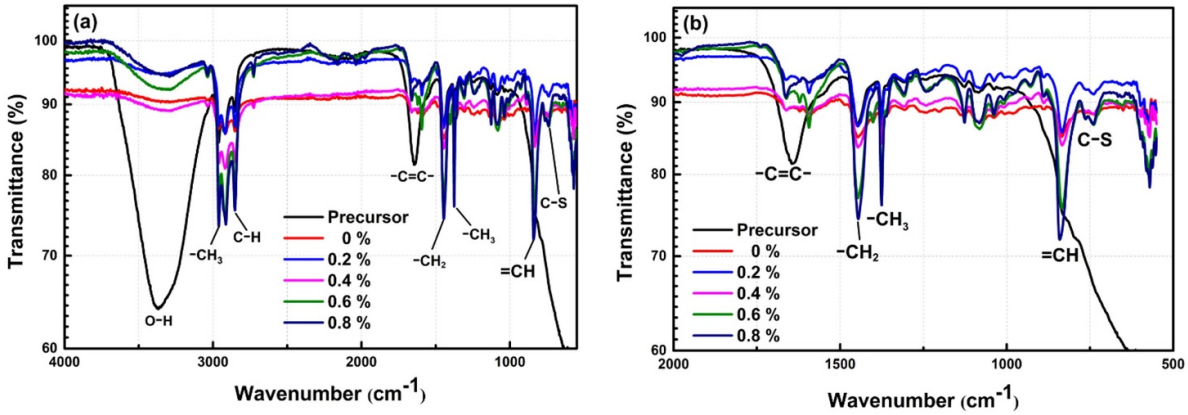

Figure 6. Comparison of FTIR transmittance spectra of (a) natural rubber latex precursor and thin films with different sulphur concentrations and (b) zoom in region at wavenumber range between 2000–500 cm^{-1}.

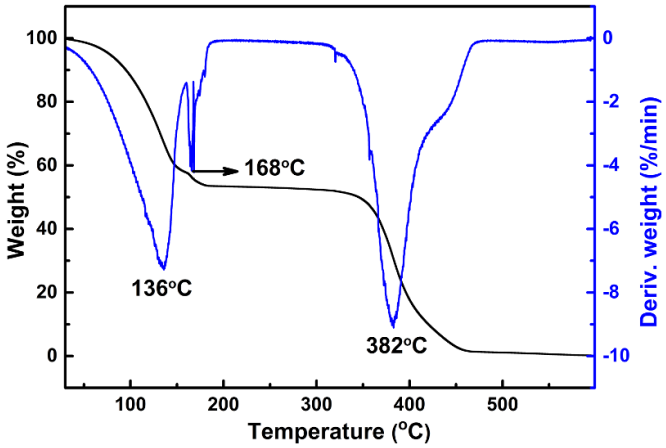

Figure 7. Thermogravimetric analysis and calculated differential thermogravimetry curve of natural rubber latex precursor solution with 0.2 wt.% sulphur.

may serve as a defect site within the active thin film if it is not passivated during the conversion from precursor solution to the dried thin film after post vulcanization and subsequently it plays a significant role in determining the RS properties of the thin film. The passivation of the sulfonium ion with the formation of polysulphide (C–S) chains (⑤) indicates that a crosslinking between long chains of NR or polyisoprene occurs when temperature (180 °C) was applied to the precursor solutions and transformed it to a dried thin film at post vulcanization process. Hence, the post-vulcanization process marks the transformation of –C=C– bonds into C–S bonds that signifies the creation of cross-linked structures [66, 73].

Figure 6(a) compares the FTIR transmittance spectra of NR precursor solution and thin films dried at 180 °C with different concentrations of sulphur. It is essential to highlight that the TGA results in figure 7 confirm that the NR is thermally stable at 180 °C. Consequently, the choice of utilizing 180 °C for the drying process is well-founded, as this temperature facilitates efficient removal of moisture [75], water [76], proteins and fatty acids residues [77], without triggering significant thermal degradation of the NR latex precursor solution. From the FTIR result in figures 6(a) and (b), there is a noticeable change in the intensity of spectral bands ranging from 800–3400 cm^{-1} for thin films if compared with precursor solution. Additional functional group of C–S (⑤) is revealed in thin film and reduction of –OH band results from the evaporation and dehydration of water and/or the removal of residual from the NR (①) during polymerization at post vulcanization process. The transformation of –C=C– bonds into C–S bonds is a pivotal factor in modulating the RS characteristics of the devices. The –C=C– bonds (①) are characteristic of conjugated systems, where alternation of single and double bonds permits the delocalization of electrons across the structure and enhances charge transport capabilities [78, 79]. Simultaneously, the formation of C–S bonds (⑤) indicates that a crosslinking of forming a three-dimensional (3D) network structure of NR may occur, but it requires the breaking of –C=C– bonds for this formation. Hence, with the formation of the 3D networks of NR, it may impact on the RS characteristics of the thin film. These C–S bonds can change the dynamics of electron interactions,

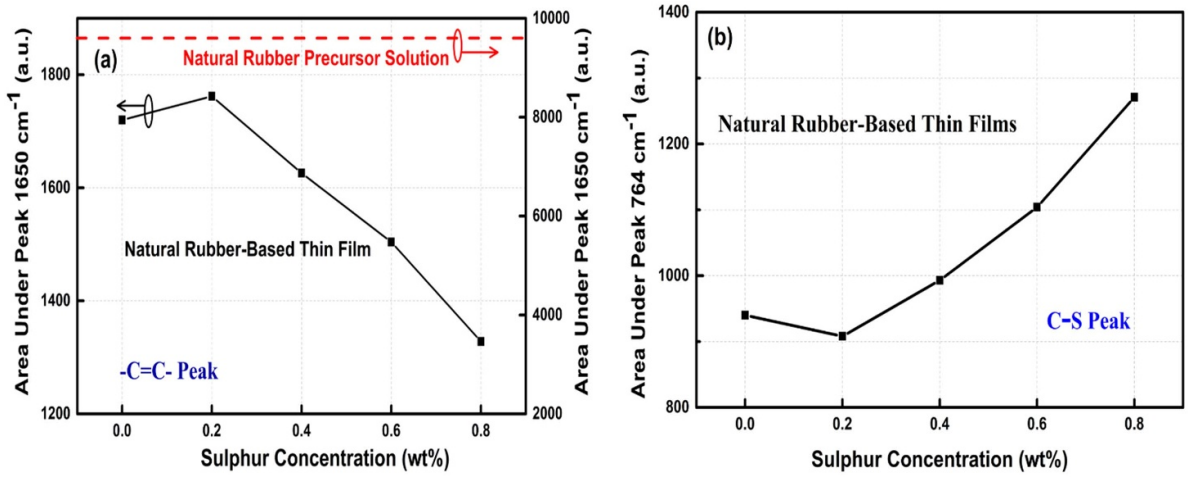

Figure 8. Area under FTIR peak at (a) 1650 cm^{-1} and (b) 764 cm^{-1} that is associated with –C=C– and C–S functional groups, respectively, as a function of sulphur concentration.

particularly at the interface between an electrode and the active NR thin film. These changes are crucial as they can influence charge trapping and transport mechanisms, which are essential to the functionality of the RS devices.

To comprehensively examine the relationship of –C=C– and C–S bonds as a function of sulphur concentration in thin film, the concentrations were determined from the area under the respective transmittance peaks from FTIR (figures 8(a) and (b)). Initially, with no sulphur in the isoprene, –C=C– bonds remain intact and unchanged (sequence ⑥ in figure 9). By increasing the sulphur concentration up to 0.2 wt.%, an increment in the concentration of –C=C– bonds is recorded but a reduction trend is observed when the concentration of sulphur is beyond 0.2 wt.% and until it reaches 0.8 wt.% (figure 8(a)). At 0.2 wt.% of sulphur concentration, the amount of sulphur may be insufficient to effectively initiate cross-linking within the isoprene chains. During the vulcanization process, sulphur becomes chemically active and some of the sulphur-sulphur bonds in the sulphur chains may temporarily break up and form free radicals (⑥). These free radicals can induce certain level of chain scission in the polyisoprene and form additional –C=C– bonds at the points where the chains are disrupted (⑦). Beyond 0.2 wt.% with further increases of sulphur concentration, the reduction of concentration in –C=C– bonds (figure 8 (a)) is attributed to the formation of more C–S bonds (⑧). As more sulphur is introduced, it allows additional cross-linking reaction within the polyisoprene chains. This is supported by the opposite trend recorded in C–S concentration as a function of sulphur concentration (figure 8(b)). Consequently, the dried thin film with 0.2 wt.% of sulphur has higher concentration of –C=C– bonds with less 3D network structure formation and higher amount of defect sites (S^+) within the thin film if compared to the thin film with sulphur concentration higher than 0.2 wt.%.

The surface roughness of NR thin films with various sulphur concentrations was measured by AFM. The average (R_a) and root-mean-square (R_{rms}) roughness in response to the sulphur concentrations is shown in figure 10. A notable increasing trend in both R_a and R_{rms} was observed with the increment of sulphur concentration. The linear increment trend of the surface roughness as a function of sulphur concentration does not fit well with the trend of cross-linking formation (figure 8) with the addition of sulphur. This indicates that the cross-linking happens within the bulk of the NR and therefore does not directly affect the surface roughness.

A typical current density-voltage (J–V) characteristic curve of a test structure with NR-thin film of 0.2 wt.% sulphur is shown in figure 11. A sweeping voltage was applied to the top electrode while the BE was grounded and current was measured. The current density (J) was calculated by dividing measured current (I) with cross-sectional area (A) of the top electrode. The compliance current was set at 1 mA to prevent the NR thin film to breakdown. The voltage was swept in the following sequence: 0 V to 4 V, 4 V to 0 V, 0 V to −4 V, and −4 V to 0 V. When the voltage was swept positively (sequence ① in figure 11), up to 2.5 V, a low current density of 10^{-4} A cm^{-2} was recorded and it is defined as OFF state or high resistance state (HRS). As the voltage was beyond 2.5 V, which is defined as SET voltage, an abrupt increment in current density was recorded (②). This high current density level is known as ON state or low resistance state (LRS). The transition from an OFF to an ON state at the SET voltage is referred to the writing process of a memory device. With the further increment of voltage, current remains stable till 4 V. As the bias continues to increase (③), the current density remains constant at compliance until it reaches 4 V. In the subsequent step, a reverse voltage sweep was applied from 4 V to 0 V (④). The device remains relatively stable in the ON state, maintaining a high current flow. As the reverse voltage approached 0 V, a notable change in current density was observed. However, this level of current density remains significantly higher (nearly three orders of magnitude) if compared to the initial value of 0 V.

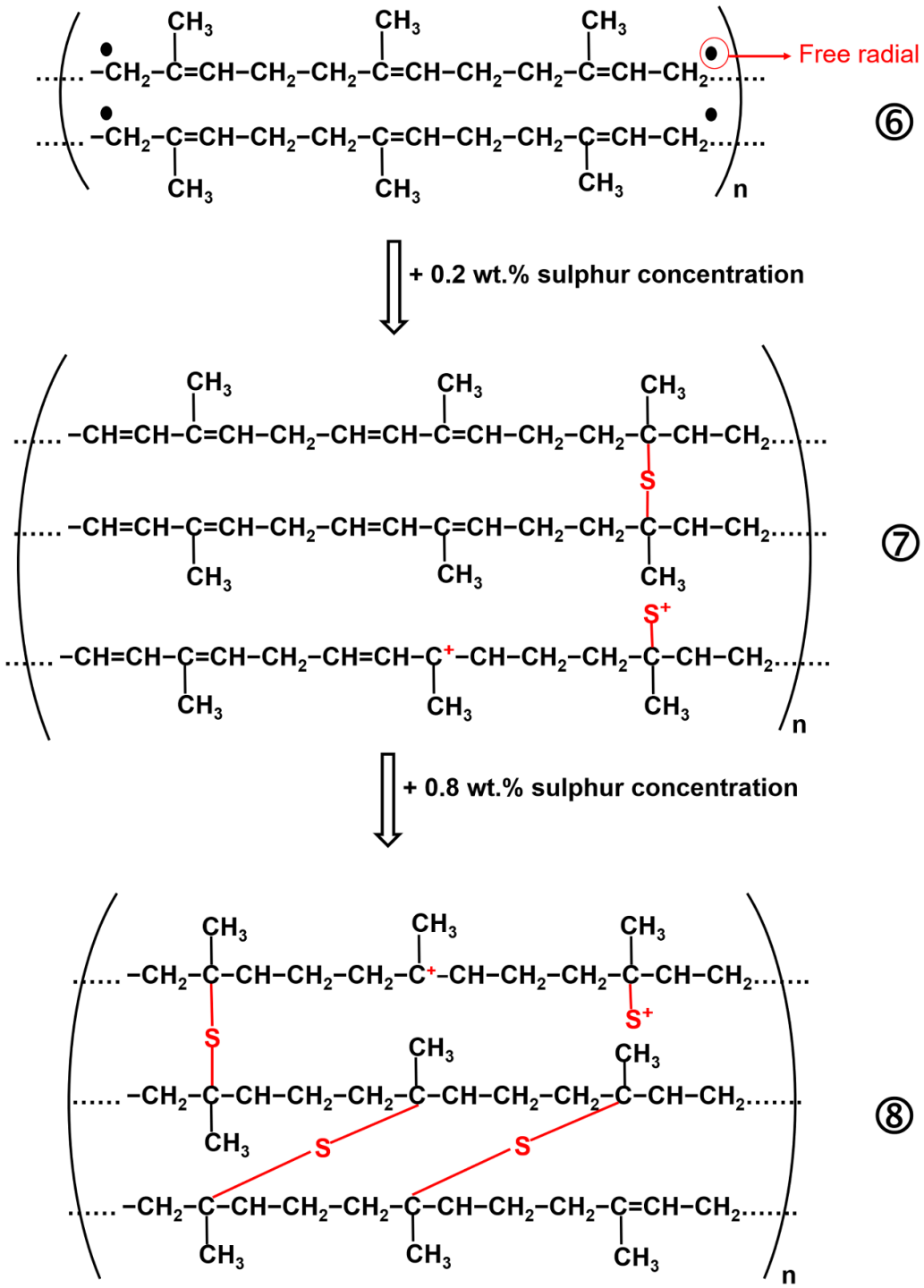

Figure 9. Detailed schematic of chemical reactions in the vulcanization process of natural rubber.

This behavior suggests that the active layer retains charged even at a flat-band voltage. When the applied voltage is swept negatively from 0 V to −4 V (⑤), the current density initially increases and then returns to the same level recorded in the previous sweep, keeping the device in the ON state. As the sweep continued from −4 V back to 0 V, the device maintained its stability until it reached a reverse bias of −3 V (⑥). At this point, the current density suddenly dropped, within a narrow range of voltage (−3 V to −2.5 V), from approximately 10^{-1}–10^{-4} A cm^{-2}, indicating that the device had switched back to the OFF state (⑦). The threshold voltage at −3 V transited the device from ON to OFF state is called RESET voltage (V_{reset}). The current density is further reducing as the voltage keeps reducing from −2.5 V to 0 V (⑧).

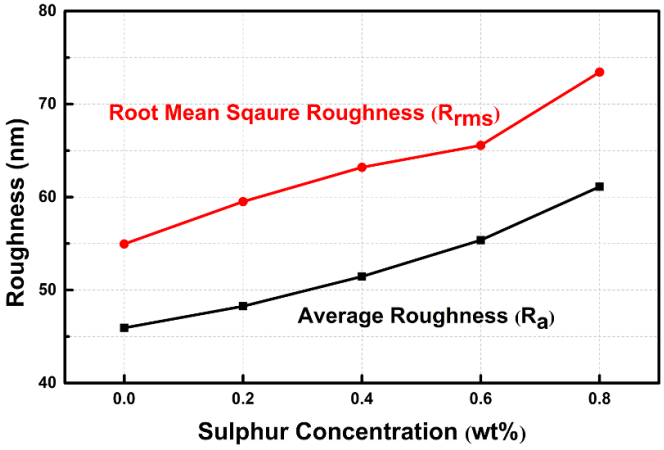

Figure 10. Root mean square roughness (R_a) and average roughness (R_{rms}) of natural rubber-based thin films as a function of sulphur concentration.

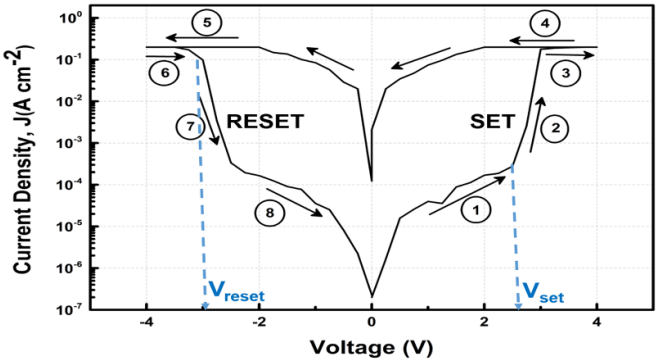

Figure 11. A typical current density-voltage (J–V) characteristics of a natural rubber-based memory device with 0.2 wt.% sulphur concentration. The directional arrows depicted in the illustration denote the direction of the voltage sweep, as indicated by the corresponding numerical values.

Figure 12 shows a representative family plot of J–V curve for samples with different concentrations of sulphur in NR thin film. All the samples with different concentrations of sulphur exhibit bipolar RS characteristics with a symmetrical nature. From the figure, the ON/OFF ratio is obtained from a read voltage of 0.25 V and memory window (figure 13(a)) is extracted from the difference between V_{SET} and V_{RESET} (figure 13(b)) as a function of sulphur concentration. The trend for these two parameters is similar to the trend of crosslinking effect as represented by C–S function group shown in figure 8(b). This indicates that the RS performance of the NR-based ReRAM is affected by the concentration of sulphur added into the NR for the formation of crosslinks and the density of trap sites contributed by S^+ (sequence ⑦ and ⑧ in figure 9) but not affected by the surface roughness of NR thin film (figure 10). Of the concentrations of sulphur added in the NR, 0.2 wt.% would be the optimum concentration that reveals the highest ON/OFF ratio with reasonable read memory window. This suggested that –C=C– in the NR is an important

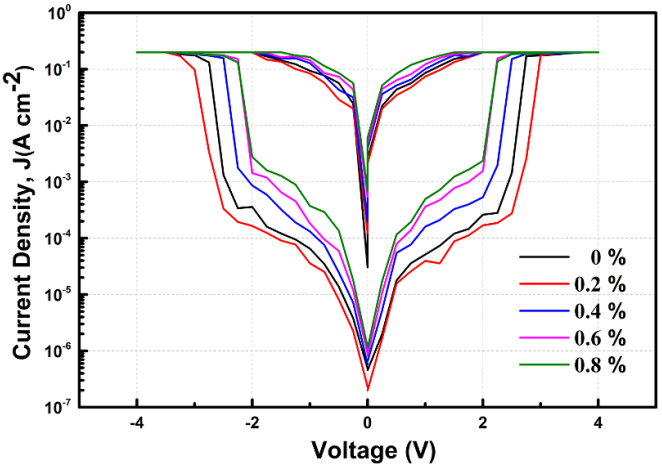

Figure 12. Resistive switching characteristic of J–V curves for natural rubber with different concentrations of sulphur.

functional group that serves as the path for electron transportation. With higher concentration of –C=C– group, electrons can transport easier and contribute to a higher current density. As a result, the ON/OFF ratio increases. The increment of –C=C– concentration is also causing an increment in defect sites within the NR such as S^+ (sequence ⑦ in figure 9). This defect sites may also contribute to the increase of the current density and attribute to the increment of the ON/OFF ratio. Therefore, the increment of –C=C– would reduce the crosslinking formation of the NR molecules. The symmetric nature of the J–V curves suggested that the RS mechanism is primarily based on electron transport through the crosslinking of the NR molecular long chain and/or network with the assistance of –C=C– function group and control by defect sites, such as S^+, within the bulk NR thin film, that is independent of voltage sweeping direction. By reversing the voltage sweeping sequences (figure 14), RS characteristic of the J–V curves with similar symmetrical nature is recorded.

The RS characteristic from the J–V curve for NR-based ReRAM with different concentrations of sulphur was transformed into double-logarithmic plots, in order to evaluate the charge conduction mechanism. The slope of the linear fits (n) and goodness of fits (r^2) of the HRS and LRS were determined and plotted for both positive and negative bias (figure 15). For both forward and reverse bias of HRS, the governing conduction mechanism at low voltages (Region A) is elucidated by either trap-filled limited and/or Mott–Gurney Law [37] as their slopes (n) values are ranging from approximately 2.03–2.41, regardless of the concentration of sulphur. However, for LRS of both forward and reverse bias (Region B), independent of the sulphur concentration, the charge conduction is governed by Ohm's law [80] as the n values are ranging between 0.88 and 1.13.

The switching of resistance from HRS (Region A in figure 15) to LRS (Region B in figure 15) is attributed to the formation of conductive paths connecting between the top and BEs. In order to identify the type of conductive path, elemental

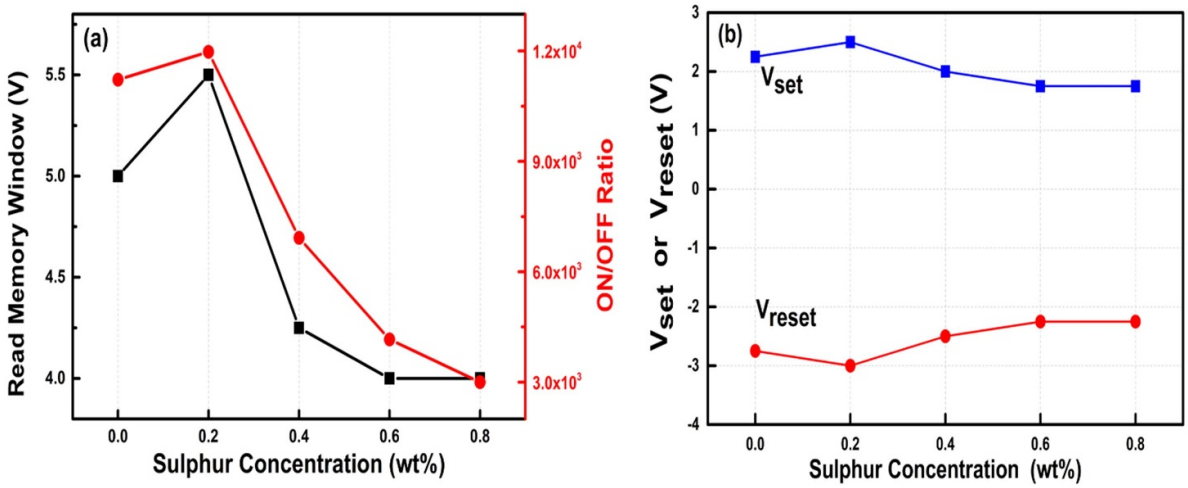

Figure 13. (a) Plots of read memory window and ON/OFF ratio and (b) V_{set} and V_{reset} as a function of sulphur concentration in natural rubber based ReRAM.

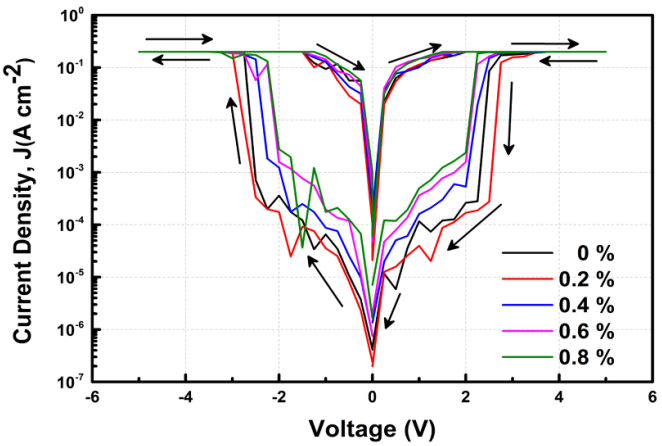

Figure 14. Resistive switching characteristic of J–V curves for natural rubber with different concentrations of sulphur in reverse bias.

chemical composition of the NR thin film before and after the memory device has been SET was evaluated. If the conductive paths are formed, the paths must connect between the top and BEs. Therefore, distribution of elemental chemical composition measured by EDS attached to TEM was only confirmed to the NR thin film deposited on BE of ITO. Figure 16 compares the elemental chemical distribution of NR-based ReRAM with 0.2 wt.% of sulphur in a pristine (figures 16(a) and (b)) and LRS after the device was SET (figures 16(c) and (d)). The measurement was conducted from the ITO electrode towards NR-based thin film, as indicated by the upward arrows in the TEM images. As shown in the elemental chemical distribution, only C and O are detected in the NR thin film for both samples with no significant difference in their concentrations. This indicates that neither Ag from the top electrode or In and Sn from BE, contributed to the conductive paths connecting between the two electrodes and therefore switched the memory device from HRS to LRS. As a result, it can rule out that the RS is governed by the formation of metallic filaments due to electrochemical process of the electrodes.

The RS characteristics of the NR-based memory device can be explained schematically using band diagrams as shown in figure 17. The sequence (①–⑧) of the band diagrams corresponds to the switching behavior depicted in the J–V curve of figure 11. The work functions of the top (Ag) and bottom ITO electrodes, relative to the vacuum level, are 4.3 and 4.7 eV, respectively [81]. The pristine memory device contains defect or trap sites (S^+) within the bulk NR thin film (①) as indicated in figure 9 (sequence ⑦ and ⑧). During the initial stage, a positive voltage is applied to the top electrode, while the BE is set to a negative bias. Due to higher work function of ITO if compared with Ag, electrons can inject from the ITO through the bulk NR thin film to the Ag electrode (②). These electrons are transported through –C=C– bonds within the NR molecules (sequence ⑦ and ⑧ in figure 9) and facilitated by the trap sites (S^+) within the bulk NR. The positively charged trap sites enable the trapping and detrapping of electrons that can be drifted towards the positively applied voltage at the Ag electrode and attributed to the change in resistance from a HRS to LRS. This is known as the SET process, where the

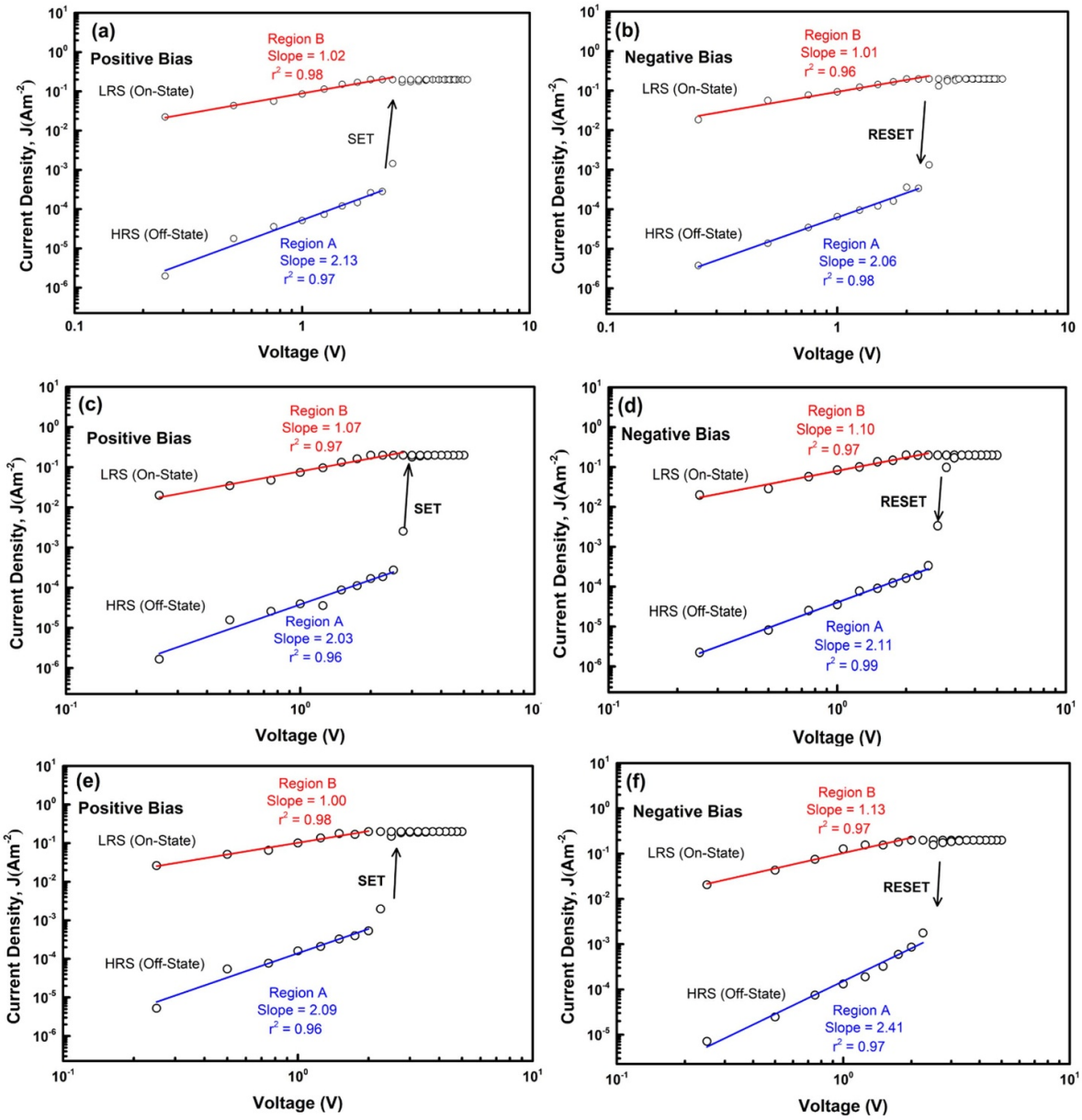

Figure 15. Double-logarithmic plots of J–V for natural rubber-based ReRAM with sulphur concentrations of (a)–(b) 0 wt.%, (c)–(d) 0.2 wt.%, (e)–(f) 0.4 wt.%, (g)–(h) 0.6 wt.%, and (i)–(j) 0.8 wt.%. The positive bias plots are indicated as (a), (c), (e), (g), and (i) while the negative bias plots are labeled as (b), (d), (f), (h), and (j). The experimental data is represented by open circles and solid lines show the linear fitting of the data. The slope of the linear fit and goodness of fit are denoted by n and r^2, respectively.

data is stored. As the positive bias increases further, more electrons are injected from the ITO electrode to fill the traps that have been detrapped due to the escape of electrons towards the top Ag electrode. Therefore, electrons can move from the ITO electrode, drift through the NR layer via randomly distributed trap centers assisted by –C=C– bonds and reach the positively biased Ag electrode (③,④). When the voltage is reversed and a negative bias is applied, making the Ag electrode more negative than the ITO electrode, the direction of the electron movement is reversed. Electrons are now injected from the Ag electrode and moving towards the ITO electrode. Their movement, still facilitated by –C=C– bonds and trap sites, involves trapping and detrapping (⑤, ⑥). As the negative bias continues, electrons begin to accumulate within the trap sites (⑦). The trapped electrons create a repulsive force that prevents further injection of electron from the Ag electrode and effectively blocking any additional electrons from entering the NR. This led to a substantial reduction in electron flow across the NR and reverting the device to its original HRS (⑧).

This dynamic of charge trapping and detrapping is further corroborated by the TEM images of the pristine memory (figure 18(a)) and memory being SET (figure 18(b)). It can be seen that during the pristine state, the NR thin film with uniform morphology if compared with the SET memory which reveals small patches of structures distributed within the thin film. This change in appearance is likely attributable to the

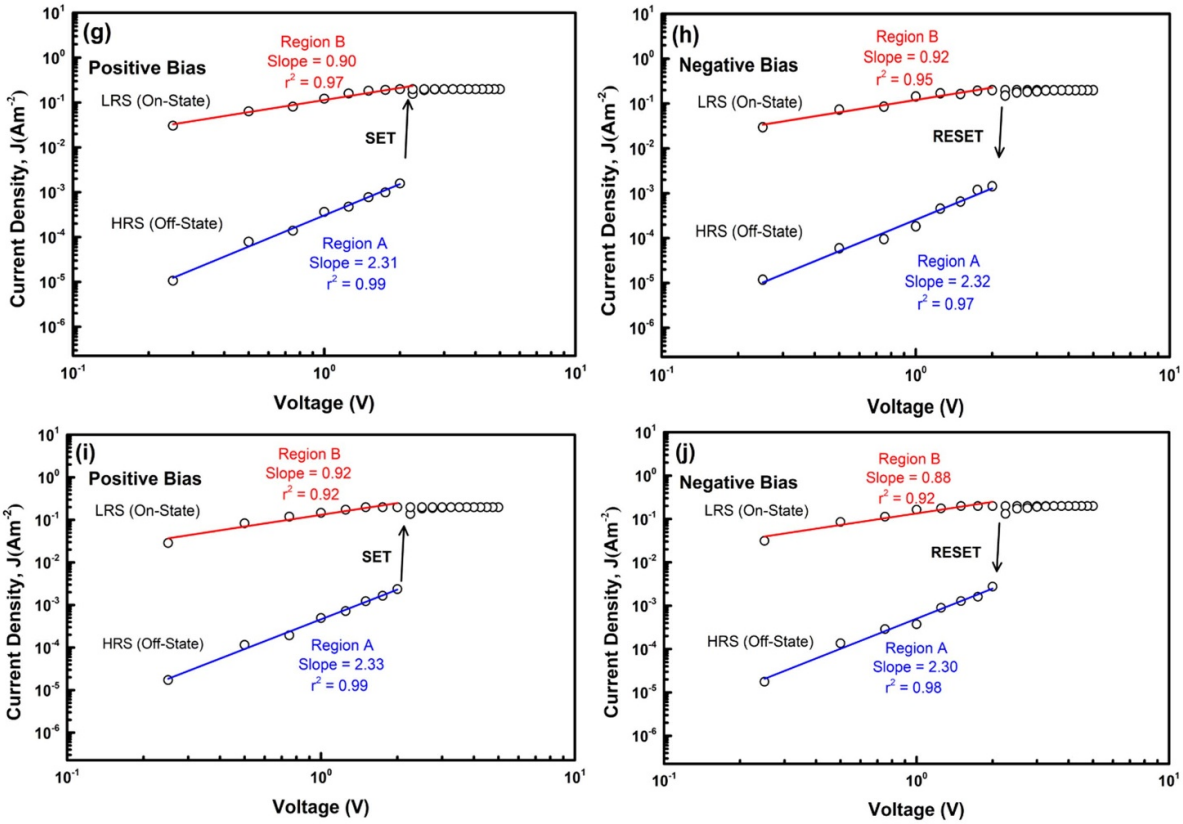

Figure 15. (Continued.)

formation of defect sites and the migration of electrons within the thin film. In order to confirm the proposed RS mechanism, Ag top electrode was replaced by a higher work function of Au (5.1 eV) [82]. The J–V curves of ReRAM with Ag and Au as top electrode on 0.8 wt.% of sulphur in NR are compared (figure 19). A smaller magnitude of V_{set} and V_{reset} is recorded in sample with Au electrode than Ag electrode. The higher work function of Au may imply that less voltage is needed for electron to transport from one electrode to another, contributing to the observed differences in switching characteristics.

Stability of the memory device was determined using a data retention test at room temperature with a read voltage of 0.5 V (figure 20(a)). It was found that both resistance states are stable for 10^4 s without experiencing any degradation. The current stability in both ON and OFF states is expected to be consistent throughout the 10 year period and confirms the excellent non-volatile nature of the device. An endurance test was also conducted to confirm the repeatability of the RS between ON and OFF states for 120 cycles on a same device. The performance of the device after 120 cycles is considered stable as shown in the J–V curve (figure 20(b)). The distribution of V_{set} and V_{reset} extracted from the figure is narrow with good consistency (figure 20(c)).

Figure 20(d) shows the typical I–V curves of the test devices measured at different sweep rates. At a high sweep rate of 0.25 V s^{-1}, the I–V curve exhibits a relatively sharp transition between the HRS and LRS, with noticeable but less pronounced RS if compared with lower sweep rates. At the lowest sweep rate of 0.001 V s^{-1}, the I–V curve displays the most stable RS behavior between HRS and LRS, with the slow sweep rate allowing the device to fully respond to the applied voltage and resulting in the most reliable switching characteristics. Overall, as the sweep rate decreases, the memristor exhibits a more stable and distinguishable switching state, indicating a better performance with slower sweep rate that allows more time for the switching processes to occur. Additionally, the effect of compliance current on the RS behavior had been reported in [83], demonstrates that the higher compliance currents (e.g. 10 mA) result in more pronounced conductive states indicating that our device can maintain multiple conductive states reliably. With a lower compliance current, it demonstrated a clear switching behavior, albeit at a reduced current level. In this research, we have achieved a high ON/OFF ratio of 10^4 and good endurance of 120 cycles, aligning well with, and are competitive in, the current landscape of bio-organic materials. To date, the ON/OFF ratios for these materials typically range from 10^1 to 10^7, with most reported values falling between 10^2 and 10^3 [17, 27, 38, 48, 52]. Similarly, the endurance cycles for bio-organic materials generally span from 10^1 to 10^3, with the majority around 10^2 [17, 28, 29, 38, 48, 52].

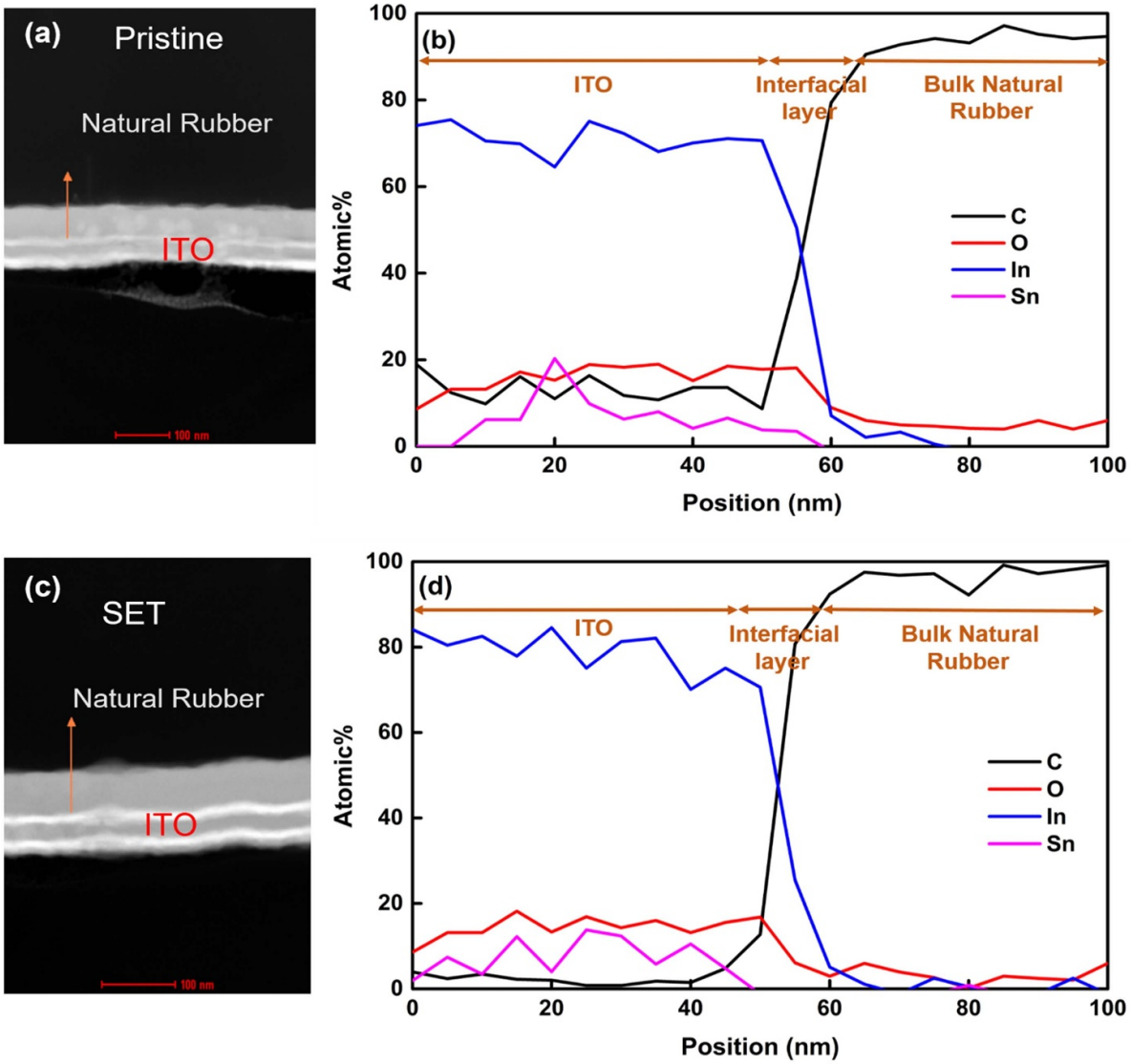

Figure 16. Elemental chemical distribution obtained from EDS with cross-sectional TEM images of for (a) pristine and (c) after SET to LRS for natural rubber thin film with 0.2 wt.% sulphur. Arrows in the TEM images show the direction of the corresponding EDS line scan presented in (b) and (d), respectively.

7. Conclusions

This research elucidates the effect of varying sulphur concentrations (0–0.8 wt.%) on the RS characteristics of NR thin films and highlighted their potential for ReRAM applications. The study involved the fabrication of NR-based thin films, achieved through the drop-casting of a precursor solution with different sulphur concentrations, followed by a drying process at 180 °C for 30 min. The resulting memory devices were fabricated using a metal–NR–metal structure, employing Ag and ITO as the top and BEs, respectively. A key finding of this study is the critical role of sulphur concentration in the NR, which directly affects the degree of crosslinking within the material. The RS performance of the fabricated memory devices was observed to be closely linked to the degree of crosslinking. The presence of functional groups, such as –C=C– and C–S, in the NR thin films was found to govern the extent of crosslinking and the formation of defect sites (S^+). Intriguingly, a lower degree of crosslinking, implying a higher concentration of –C=C– bonds and S^+ defect sites that enhanced the RS behavior of the memory devices. The study revealed that the switching mechanism between high and LRSs was governed by the formation of conductive paths due to electron transport along the –C=C– bonds and S^+ defect sites connected between the top and BEs. With 0.2 wt.% of sulphur in the NR thin film, the memory device exhibited remarkable RS performance: a high ON/OFF ratio of 10^4, a substantial memory window of 5.5 V, prolonged data retention that was extrapolated up to 10 years, and reliable endurance over 120 cycles. Therefore, this research demonstrates the potential of NR as an innovative and promising material for the advancement of next-generation ReRAM applications.

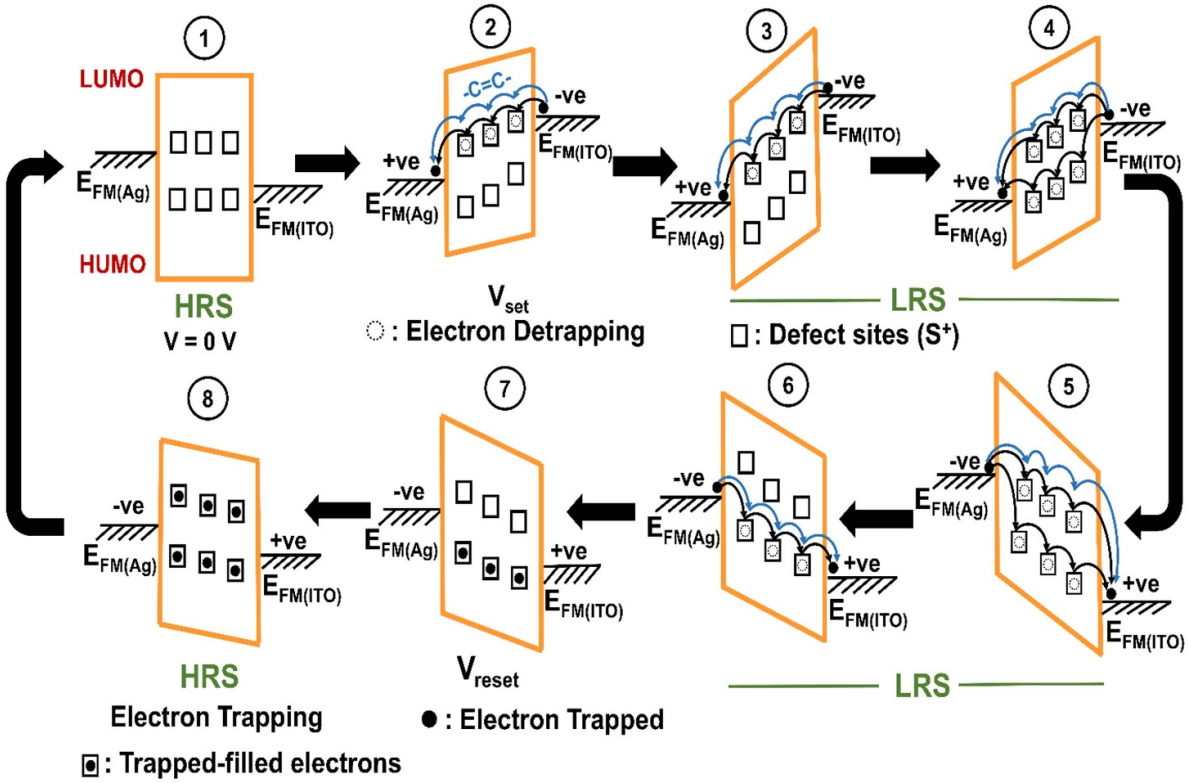

Figure 17. Schematic of the proposed resistive switching mechanism of natural rubber-based ReRAM.

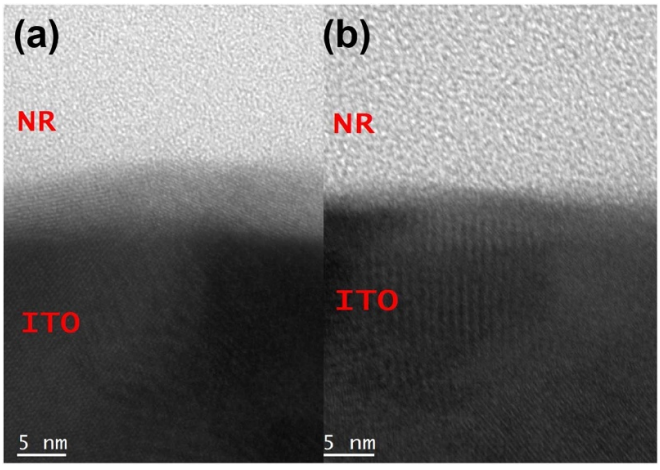

Figure 18. TEM images of the cross-sectional interfacial region between the natural rubber thin film and ITO for (a) pristine and (b) SET memory.

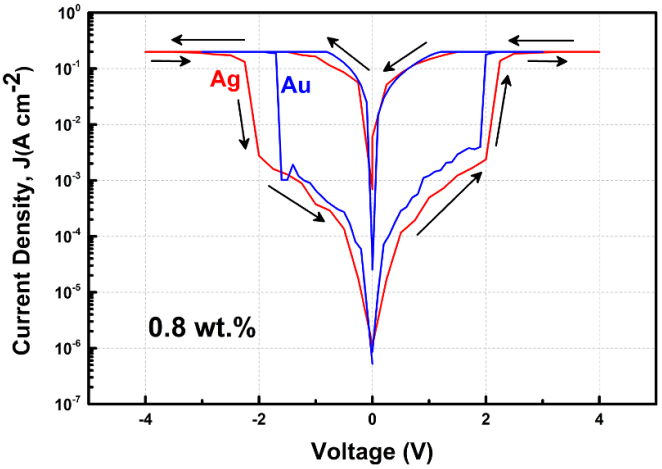

Figure 19. Resistive switching characteristic of J–V curves for ReRAM with Au and Ag as top electrode on natural rubber with 0.8 wt.% of sulphur.

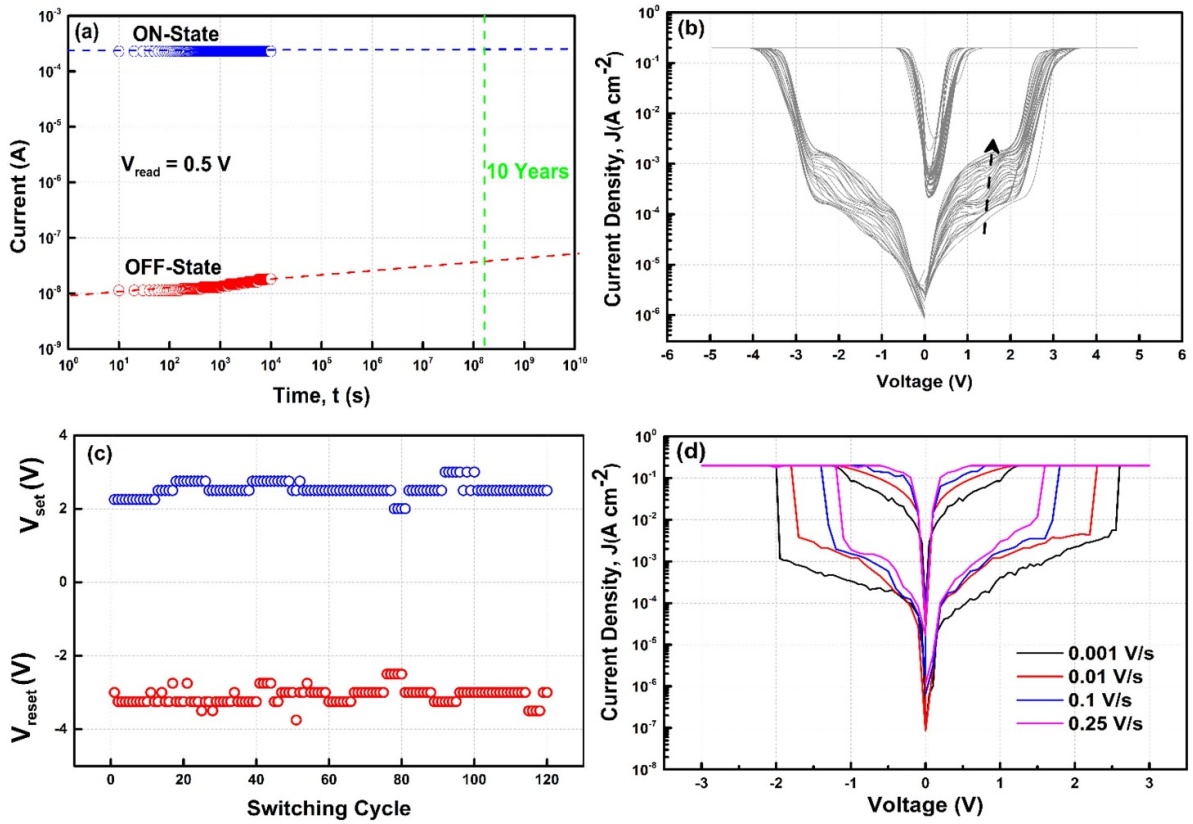

Figure 20. (a) Retention characteristics of ON and OFF states measured at $V_{read} = 0.5$ V, (b) J–V characteristics of the natural rubber-based device with 0.8 wt.% of sulphur. 120 switching cycles were recorded, shown as individual grey curves. The dotted arrow represents the progression of cycles, ranging from 0 to 120, (c) distribution of V_{set} and V_{reset} values of the test structure over 120 switching cycles and (d) typical I–V curves of Ag/natural rubber/ITO device measured at different sweep rates.

Data availability statement

Reference to the datasets analyzed during the current study are available from the corresponding author on reasonable request.

The data that support the findings of this study are available upon reasonable request from the authors.

Acknowledgments

K Y C would like to acknowledge the financial support by the Fundamental Research Grant Scheme (FRGS/1/2021/TK0/USM/01/5) (PBAHAN.6071499) under the Ministry of Higher Education, Malaysia. F Z acknowledges the support by the US National Science Foundation under Grants 2104976 and 2247342.

Authors contributions

All authors contributed equally to this work.

Conflict of interest

The authors declare that they have no known competing financial interests or personal relationships that could have appeared to influence the work reported in this paper.

ORCID iDs

Muhammad Awais https://orcid.org/0000-0002-7246-9313
Feng Zhao https://orcid.org/0000-0001-9350-6497
Kuan Yew Cheong https://orcid.org/0000-0001-8049-0297

References

[1] Roldán J B *et al* 2023 Variability in resistive memories *Adv. Intell. Syst.* **5** 2200338
[2] Li Y, Qian Q, Zhu X, Li Y, Zhang M, Li J, Ma C, Li H, Lu J and Zhang Q 2020 Recent advances in organic-based materials for resistive memory applications *InfoMat* **2** 995–1033
[3] Wang J, Sun B, Zhou G, Zhu S, Yang C, Ke C, Zhao Y and Wang H 2023 Nonvolatile resistive switching memory behavior in WOx/BiFeOy heterojunction based memristor *J. Alloys Compd.* **939** 168761
[4] Dilna U and Prasad S N 2024 An efficient in-memory carry select adder realization using resistive switching crossbar array with Ti-doped VO2 -based selector device *Mater. Sci. Semicond. Process.* **171** 108008
[5] Awais M, Zhao F and Cheong K Yew 2023 Bio-organic based resistive switching random-access memory *SSP* **352** 85–93
[6] Sharma P K, Prasad S S, Tasneem S, Priyadarshini B and Ranjan R K 2023 Resistive tunable memristor emulator model and its application *AEU-Int. J. Electron. Commun.* **160** 154500
[7] Xie Y and Zhao Y 2019 Emerging memory technologies *IEEE Micro* **39** 6–7
[8] Gao S, Yi X, Shang J, Liu G and Li R W 2019 Organic and hybrid resistive switching materials and devices *Chem. Soc. Rev.* **48** 1531–65
[9] Sueoka B, Cheong K Y and Zhao F 2022 Study of synaptic properties of honey thin film for neuromorphic systems *Mater. Lett.* **308** 131169
[10] Ielmini D 2018 Brain-inspired computing with resistive switching memory (RRAM): devices, synapses and neural networks *Microelectron. Eng.* **190** 44–53
[11] Meena J S, Sze S M, Chand U and Tseng T Y 2014 Overview of emerging nonvolatile memory technologies *Nanoscale Res. Lett.* **9** 1–33
[12] Shi C, Wang J, Sushko M L, Qiu W, Yan X and Liu X Y 2019 Silk flexible electronics: from Bombyx mori silk ag nanoclusters hybrid materials to mesoscopic memristors and synaptic emulators *Adv. Funct. Mater.* **29** 1904777
[13] Jena A K, Sahu M C, Mohanan K U, Mallik S K, Sahoo S, Pradhan G K and Sahoo S 2022 Bipolar resistive switching in TiO_2 artificial synapse mimicking Pavlov's associative learning *ACS Appl. Mater. Interfaces* **15** 3574–85
[14] Shi T, Wang R, Wu Z, Sun Y, An J and Liu Q 2021 A review of resistive switching devices: performance improvement, characterization, and applications *Small Struct.* **2** 2000109
[15] Shaikh M T A S, Nguyen T H V, Jeon H J, Prasad C V, Kim K J, Jo E S, Kim S and Rim Y S 2024 Multilevel reset dependent set of a biodegradable memristor with physically transient *Adv. Sci.* **11** 1–11
[16] Awais M, Zhao F and Cheong K Y 2023 Bio-organic based resistive switching random-access memory *Solid State Phenom.* **352** 85–93
[17] Faita F L, Avila L B, Silva J P B, Boratto M H, Cid C C P, Graeff C F O, Gomes M J M, Müller C K and Pasa A A 2022 Abnormal resistive switching in electrodeposited Prussian White thin films *J. Alloys Compd.* **896** 162971
[18] Sokolov A S, Abbas H, Abbas Y and Choi C 2021 Towards engineering in memristors for emerging memory and neuromorphic computing: a review *J. Semicond.* **42** 013101
[19] Hu W, Yang B, Zhang Y and She Y 2020 Recent progress in physically transient resistive switching memory *J. Mater. Chem.* C **8** 14695–710
[20] Tseng R J, Tsai C, Ma L, Ouyang J, Ozkan C S and Yang Y 2006 Digital memory device based on tobacco mosaic virus conjugated with nanoparticles *Nat. Nanotechnol.* **1** 72–77
[21] Liu S J, Wang P, Zhao Q, Yang H Y, Wong J, Bin Sun H, Dong X C, Lin W P and Huang W 2012 Single polymer-based ternary electronic memory material and device *Adv. Mater.* **24** 2901–5
[22] Liu X, Shi M, Luo Y, Zhou L, Loh Z R, Oon Z J, Lian X, Wan X, Chong F B L and Tong Y 2020 Degradable and dissolvable thin-film materials for the applications of new-generation environmental-friendly electronic devices *Appl. Sci.* **10** 1320
[23] Lee J H, Park S P, Park K and Kim H J 2020 Flexible and waterproof resistive random-access memory based on nitrocellulose for skin-attachable wearable devices *Adv. Funct. Mater.* **30** 1–6
[24] Erokhin V 2020 Memristive devices for neuromorphic applications: comparative analysis *Bionanoscience* **10** 834–47
[25] Chen A *et al* 2005 Non-volatile resistive switching for advanced memory applications *IEEE Int.Electron Devices Meeting, 2005. IEDM Technical Digest* pp 746–9
[26] Li T, Xu Y, Lei M, Zhao Y, Sun B, Elshekh H, Zheng L, Zhang X and Hou W 2020 The pH-controlled memristive effect in a sustainable bioelectronic device prepared using lotus root *Mater. Today Sustain.* **7–8** 100029
[27] Arshad N, Irshad M S, Abbasi M S, Ur Rehman S, Ahmed I, Javed M Q, Ahmad S, Sharaf M and Al Firdausi M D 2021 Green thin film for stable electrical switching in a low-cost washable memory device: proof of concept *RSC Adv.* **11** 4327–38
[28] Chang Y C, Lin C H, Liu H J and Jian J C 2023 Biodegradable resistive switching devices made from carrageenan insulator and carrageenan substrate *Org. Electron.* **120** 106818
[29] Xing Y, Sueoka B, Cheong K Y and Zhao F 2021 Nonvolatile resistive switching memory based on monosaccharide fructose film *Appl. Phys. Lett.* **119** 163302
[30] Desai T R, Dongale T D, Patil S R, Tiwari A P, Pawar P K, Kamat R K and Kim T G 2021 Synaptic learning functionalities of inverse biomemristive device based on trypsin for artificial intelligence application *J. Mater. Res. Technol.* **11** 1100–10
[31] Lee C J, Chang Y C, Wang L W and Wang Y H 2017 Nonvolatile resistive switching memory utilizing cobalt embedded in gelatin *Materials* **11** 32
[32] Qin J *et al* 2024 Evolution between RS and NRS behaviors in $BiFeO_3$@egg albumen nanocomposite based memristor *Curr. Appl. Phys.* **59** 77–84

[33] Sharma S and Kaur D 2024 Memory device based on a nano-granulars and nano-worms structured MoS_2 active layer: the origin of resistive switching characteristics *Vacuum* **222** 112989

[34] Wu W, Han S T, Venkatesh S, Sun Q, Peng H, Zhou Y, Yeung C, Li R K Y and Roy V A L 2018 Biodegradable skin-inspired nonvolatile resistive switching memory based on gold nanoparticles embedded alkali lignin *Org. Electron.* **59** 382–8

[35] Park S P, Tak Y J, Kim H J, Lee J H, Yoo H and Kim H J 2018 Analysis of the bipolar resistive switching behavior of a biocompatible glucose film for resistive random access memory *Adv. Mater.* **30** 1–8

[36] Lim Z X and Cheong K Y 2018 Nonvolatile memory device based on bipolar and unipolar resistive switching in bio-organic aloe polysaccharides thin film *Adv. Mater. Technol.* **3** 1–14

[37] Tayeb I A, Zhao F, Abdullah J M and Cheong K Y 2021 Resistive switching behaviour in a polymannose film for multistate non-volatile memory application *J. Mater. Chem.* C **9** 1437–50

[38] Rahman F Y, Deb R, Sarkar S, Banik H, Uddin M J, Chakraborty S, Bhattacharjee D and Hussain S A 2023 Resistive switching behavior employing the ipomoea carnea plant for biodegradable rewritable read-only memory applications *ACS Appl. Electron. Mater.* **5** 3685–97

[39] Wang J, Shi C, Sushko M L, Lan J, Sun K, Zhao J, Liu X and Yan X 2021 Boost of the bio-memristor performance for artificial electronic synapses by surface reconstruction *ACS Appl. Mater. Interfaces* **13** 39641–51

[40] Sun B, Zhang X, Zhou G, Li P, Zhang Y, Wang H, Xia Y and Zhao Y 2017 An organic nonvolatile resistive switching memory device fabricated with natural pectin from fruit peel *Org. Electron.* **42** 181–6

[41] Tran K M, Do D P, Ta Thi K H and Pham N K 2019 Influence of top electrode on resistive switching effect of chitosan thin films *J. Mater. Res.* **34** 3899–906

[42] Lin Q, Hao S, Hu W, Wang M, Zang Z, Zhu L, Du J and Tang X 2019 Human hair keratin for physically transient resistive switching memory devices *J. Mater. Chem.* C **7** 3315–21

[43] Awais M *et al* 2024 Impact of electrical testing strategies on the performance metrics of bio-organic-based resistive switching memory *MRS Commun.* **14** 653

[44] Mao S, Sun B, Zhou G, Yang Y, Zhao H, Zhou Y, Chen Y and Zhao Y 2022 Analog-to-digital and self-rectifying resistive switching behavior based on flower-like δ-MnO_2 *Appl. Surf. Sci.* **595** 153560

[45] Swathi S P and Angappane S 2022 Digital and analog resistive switching in NiO-based memristor by electrode engineering *Jpn. J. Appl. Phys.* **61** SM1009

[46] Min J-G, Park H and Cho W-J 2022 Milk–Ta_2O_5 hybrid memristors with crossbar array structure for bio-organic neuromorphic chip applications *Nanomaterials* **12** 2978

[47] Sueoka B, Cheong K Y and Zhao F 2022 Natural biomaterial honey-based resistive switching device for artificial synapse in neuromorphic systems *Appl. Phys. Lett.* **120** 0–6

[48] Cheong K Y, Tayeb I A, Zhao F and Abdullah J M 2021 Review on resistive switching mechanisms of bio-organic thin film for non-volatile memory application *Nanotechnol. Rev.* **10** 680–709

[49] Raeis-Hosseini N and Lee J S 2017 Resistive switching memory using biomaterials *J. Electroceram.* **39** 223–38

[50] Sawa A 2008 Resistive switching in transition metal oxides *Mater. Today* **11** 28–36

[51] Zahoor F, Hussin F A, Isyaku U B, Gupta S, Khanday F A, Chattopadhyay A and Abbas H 2023 Resistive random access memory: introduction to device mechanism, materials and application to neuromorphic computing *Discover Nano* **18** 36

[52] Rahmani M K, Khan S A, Kim H, Khan M U, Kim J, Bae J and Kang M H 2023 Demonstration of high-stable bipolar resistive switching and bio-inspired synaptic characteristics using PEDOT:PSS-based memristor devices *Org. Electron.* **114** 106730

[53] Yeoh J Z, Awais M, Zhao F and Cheong K Y 2024 Effects of silver nanoparticles in pectin polysaccharide thin film on resistive switching characteristics *J. Electron. Mater.* **53** 7071–84

[54] Tao H, Kaplan D L and Omenetto F G 2012 Silk materials—a road to sustainable high technology *Adv. Mater.* **24** 2824–37

[55] Yap P L, Cheong K Y, Lee H L and Zhao F 2022 Effects of drying temperature on preparation of pectin polysaccharide thin film for resistive switching memory *J. Mater. Sci. Mater. Electron.* **33** 19805–26

[56] Lim Z X and Cheong K Y 2015 Effects of drying temperature and ethanol concentration on bipolar switching characteristics of natural Aloe vera-based memory devices *Phys. Chem. Chem. Phys.* **17** 26833–53

[57] Cheong K Y, Tayeb I A and Zhao F 2022 Resistive switching characteristics of fullerene (C60) in polymannose thin film *Phys. Status Solidi* **16** 2200242

[58] Zhou G *et al* 2023 Full hardware implementation of neuromorphic visual system based on multimodal optoelectronic resistive memory arrays for versatile image processing *Nat. Commun.* **14** 1–11

[59] Bottier C 2020 *Biochemical Composition of Hevea Brasiliensis Latex: A Focus on the Protein, Lipid, Carbohydrate and Mineral Contents* (Elsevier Ltd) (https://doi.org/10.1016/bs.abr.2019.11.003)

[60] Jacob J 1993 The composition of Natural latex from hevea brasHiensis *Clin. Rev. Allergy* **11** 325–37

[61] Ho C C and Ng W L 1979 Surface study on the rubber particles in pretreated hevea latex system *Colloid Polym. Sci.* **257** 406–12

[62] Luzia K, Heloisa A, Juliana R, Floriano F, Diz E, Fabrício A, Faita L, Antonio R and Machado F 2023 Latex and natural rubber: processing techniques for biomedical applications *Braz. J. Chem. Eng.* **40** 913–27

[63] Peidayesh H, Špitalský Z and Chodák I 2022 Electrical conductivity of rubber composites with varying crosslink density under cyclic deformation *Polymers* **14** 3640

[64] Zaheer M *et al* 2020 Liquid-metal-induced memristor behavior in polymer insulators *Phys. Status Solidi* **14** 2000050

[65] Elwy A, Nasr G M, Hamza S S and Ibrahim S S 1996 Influence of gamma iradiation on the electrical conductivity of FEF/SBR loaded with different concentrations of sulphur *Polym. Test.* **15** 153–61

[66] Tamási K and Kollár M S 2018 Effect of different sulfur content in natural rubber mixtures on their thermo-mechanical and surface properties *Int. J. Eng. Res. Sci.* **4** 28–37 IJOER-FEB-2018-6 (available at: https://ijoer.com/assets/articles_menuscripts/file/IJOER-FEB-2018-6.pdf)

[67] Bošák O, Preťo J, Labaš V and Kubliha M 2019 Electrical conductivity of rubber blends containing zeolite filler *AIP Conf. Proc.* **2071** 030006

[68] Eshaghi A and Graeli A 2020 Optical and electrical properties of indium tin oxide (ITO) nanostructured thin films deposited on polycarbonate substrates "thickness effect" *Optik* **125** 1478–81

[69] Thirumoorthi M and Prakash J T J 2018 Structure, optical and electrical properties of indium tin oxide ultra thin films prepared by jet nebulizer spray pyrolysis technique *Integr. Med. Res.* **4** 124–32

[70] Bakar N H H A, Ismail J and Bakar M A 2007 Synthesis and characterization of silver nanoparticles in natural rubber *Mater. Chem. Phys.* **104** 276–83
[71] Jitsangiam P, Nusit K, Phenrat T, Kumlai S and Pra-ai S 2021 An examination of natural rubber modified asphalt: effects of rubber latex contents based on macro- and micro-observation analyses *Constr. Build. Mater.* **289** 123158
[72] Sreeja R, Najidha S, Jayan S R, Predeep P, Mazur M and Sharma P D 2006 Electro-optic materials from co-polymeric elastomer—acrylonitrile butadiene rubber (NBR) *Polymer* **47** 617–23
[73] Coran A Y 2013 Vulcanization *The Science and Technology of Rubber* edn 4 (Elsevier) pp 337–81
[74] Morand J L 1977 Chain scission in the oxidation of polyisoprene *Rubber Chem. Technol.* **50** 373–96
[75] Ibrahim S, Badri K, Thevy Ratnam C, Chee Keong C, Sham H, Noor Wadi Mat Lazim M, Ali N H M and Hisyam Mohd Yusof K 2022 Mechanical properties and thermogravimetric analysis of peroxide prevulcanized natural rubber latex induced by Co-60 γ radiation *IOP Conf. Ser.: Mater. Sci. Eng.* **1231** 012014
[76] Raveshtian A, Fasihi M, Norouzbeigi R and Rasouli S 2022 Curing and thermal degradation reactions of nano-alumina filled natural rubber latex foams *Thermochim. Acta* **707** 179108
[77] de Lima D R, Vieira I R S, Dutra da Rocha E B, Furtado de Sousa A M, Augusto da Costa A C and Furtado C R G 2023 Biodegradation of natural rubber latex films by highlighting the crosslinked bond *Ind. Crops Prod.* **204** 117290
[78] Jaiswal M and Menon R 2006 Polymer electronic materials: a review of charge transport *Polym. Int.* **55** 1371–84
[79] Fratini S, Nikolka M, Salleo A, Schweicher G and Sirringhaus H 2020 Charge transport in high-mobility conjugated polymers and molecular semiconductors *Nat. Mater.* **19** 491–502
[80] Hosseini N R and Lee J S 2015 Biocompatible and flexible chitosan-based resistive switching memory with magnesium electrodes *Adv. Funct. Mater.* **25** 5586–92
[81] Zhu S, Sun B, Ranjan S, Zhu X, Zhou G, Zhao H, Mao S, Wang H, Zhao Y and Fu G 2019 Mechanism analysis of a flexible organic memristive memory with capacitance effect and negative differential resistance state *APL Mater.* **7** 081117
[82] Akkaya A 2021 Au–Ag binary alloys on n-GaAs substrates and effect of work functions on Schottky barrier height *J. Mater. Sci. Mater. Electron.* **32** 17448–61
[83] Awais M, Othman N, Shafiq M D, Zhao F and Cheong K Y (AIP Conference Proceedings)